TU Delft

Delft University of Technology

Off-Gas System Scale-Up of HIsarna Iron-Making Process

A CFD-Based Approach

Hosseini, Ashkan; Hage, Johannes L.T.; Duiker, Arjan; Meijer, Koen; Peeters, Tim; Offerman, Erik; Yang, Yongxiang

DOI
10.1007/s11663-022-02620-4

Publication date
2022

Document Version
Final published version

Published in
Metallurgical and Materials Transactions B: Process Metallurgy and Materials Processing Science

Citation (APA)
Hosseini, A., Hage, J. L. T., Duiker, A., Meijer, K., Peeters, T., Offerman, E., & Yang, Y. (2022). Off-Gas System Scale-Up of HIsarna Iron-Making Process: A CFD-Based Approach. *Metallurgical and Materials Transactions B: Process Metallurgy and Materials Processing Science*, *53*(6), 3557-3574. https://doi.org/10.1007/s11663-022-02620-4

Important note
To cite this publication, please use the final published version (if applicable).
Please check the document version above.

Copyright
Other than for strictly personal use, it is not permitted to download, forward or distribute the text or part of it, without the consent of the author(s) and/or copyright holder(s), unless the work is under an open content license such as Creative Commons.

Takedown policy
Please contact us and provide details if you believe this document breaches copyrights.
We will remove access to the work immediately and investigate your claim.

This work is downloaded from Delft University of Technology.
For technical reasons the number of authors shown on this cover page is limited to a maximum of 10.

ORIGINAL RESEARCH ARTICLE

Off-Gas System Scale-Up of HIsarna Iron-Making Process: A CFD-Based Approach

ASHKAN HOSSEINI, JOHANNES L.T. HAGE, ARJAN DUIKER, KOEN MEIJER, TIM PEETERS, ERIK OFFERMAN, and YONGXIANG YANG

For all industrial applications, predicting system characteristics and behavior plays a vital role before constructing costly and complex multi-physic systems. Correct and reliable predictions become even more important once the aim is to go from small- to large-scale processes to establish an industrial demonstrations. In this study, a CFD-based scale-up of HIsarna off-gas system based on the Eulerian–Lagrangian approach is investigated and detailed step in scale-up procedure is discussed. A three-dimensional CFD model is developed and validated based on the available pilot scale data and used to design and scale up the post-combustion chamber (also known as reflux chamber). Detailed kinetics for volumetric and gas–solid reactions are incorporated in validated CFD model with a special attention to the wall boundary condition and modeling. The effect of reflux chamber geometry, oxygen injection ports, oxygen injection flowrate, isolation wall thickness, and inlet flue gas composition on different system characteristics such as heat loss through the wall, $CO–H_2$–carbon mixture conversion, flue gas, and wall temperature are investigated. The aim of the scaled up geometry, like pilot scale, is to achieve full combustion of unwanted species inside the reflux chamber to assure zero emissions from the off-gas system. Compared to the pilot scale, the scaled up reflux chamber is capable of handling and removing higher amount of unwanted species coming from the main reactor and therefore lower $CO–H_2$ and carbon particle emissions, mainly due to a larger size which provides larger volume and residence time for volumetric and gas–solid reaction to proceed.

https://doi.org/10.1007/s11663-022-02620-4
© The Author(s) 2022

I. INTRODUCTION

THE goal of scale-up is to successfully produce a desired product at a commercial scale[1] which indeed is one of the most challenging engineering tasks. Moving from one scale to another, one must understand how size changes impact a number of physical and chemical phenomena. This understanding is of outmost importance since similar yields and conversions need to be achieved in both large and small scale. Therefore, changing the construction and operating parameters (during scale-up procedure) might be a necessary to maintain the same achieved performance in smaller scale.

Scale-up procedure usually starts from ''laboratory scale'' (lab scale) in which fundamental questions about the process, such as different phasic interactions, flow properties, production efficiency, and so on are investigated and feasibility of a process is determined. The process then is scaled up to a ''pilot scale,'' to study operational parameters and to avoid risk of direct scaling to full scale. In some cases, before going to full commercial scale, scale-up from pilot to ''demonstration scale'' (demo scale) might be necessary. Compared to pilot scale, demo scale closely resembles the equipment and operating conditions of industrial scale which is the final step in the scaling-up process. Within demo scale, it is also possible to produce significant quantities of final product for market testing to determine its success. Finally, the industrial scale (commercial scale) is constructed by using research findings and operational experience from previous scales.

ASHKAN HOSSEINI, ERIK OFFERMAN, and YONGXIANG YANG are with the Department of Materials Science and Engineering, Delft University of Technology, 2628 CN Delft, The Netherlands. Contact e-mail: a.hosseini-1@tudelft.nl JOHANNES L. T. HAGE, ARJAN DUIKER, KOEN MEIJER, and TIM PEETERS are with the Tata steel IJmuiden, 1951 JZ Velsen-Noord, The Netherlands.

Manuscript submitted May 12, 2022; accepted August 5, 2022.
Article published online September 2, 2022.

Scaling-up procedure becomes even more important for new emerging and low-carbon technologies which are mostly at their early stage of development. Iron and steel production industry is one of the sectors with the largest CO_2 footprint. The main route to produce and meet the steel market need is through blast furnace technology. *Via* this technology, every ton of produced steel emitted on average 1.85 tons of carbon dioxide from 2018 to 2020. In 2020, with total production of 1,860 million tonnes of steel, total direct emissions from this sector were of the order of 2.6 billion tonnes, representing 7 to 9 pct. of global anthropogenic CO_2 emissions. If we counted the emissions of the steel industry as if it were a nation, it would rank the 5th largest CO_2-producing nation in the world.[2–4]

There is a growing interest in developing innovative ways of steel production to meet CO_2 and other pollutant emission requirements. Among them, HIsarna process has drawn researchers and investors' attention and shown promising results to be fully scaled up to industrial scale.

The process is a combination of the Cyclone Converter Furnace (CCF) and the HIsmelt technology. The main reactor, off-gas system, and other upstream components are shown in Figure 1.

Via this new route, it is possible to produce hot iron directly from coal and dine iron ore. Therefore, the intermediate process of coking and sintering step are eliminated which inherently lead to a 20 pct reduction of CO_2 emission. Further CO_2 emission reduction, up to 80 to 90 pct, can be achieved by incorporating carbon capture technologies.

The main reactor can be divided into two sections. Fine iron ore and oxygen are injected into the CCF. The oxygen combusts the CO–H2 mixture coming from CCF to provide enough heat to pre-reduce and melt the fine ore particles. The molten particles hit the wall and create a molten film which drips into the SRV where final reduction step to pure iron takes place *via* reacting with the injected coal into the slag. The outlet gas from CCF mainly is a mixture of CO_2–H_2O–N_2 with small amount of CO, H_2, O_2, and carbon particles which enter the off-gas system for post-combustion as will be discussed in Section II.

The current HIsarna plant is built in pilot scale, capable of producing 60,000 tons hot metal per year (thm/yr) in the IJmuiden Works of Tata Steel Europe in 2010 and since that time, it has been under development toward industrial demonstration. The scale-up of this pilot plant to demo and industrial scale will be built in Jamshedpur, India, with a capacity of 400,000 thm/year and 1 million thm/year, respectively. Figure 2 shows schematic view of the main reactor for different scales.

Traditionally, dimensionless numbers and experimental correlations have been utilized for sizing of a scaled unit. However, using traditional methods requires extrapolating beyond the experimental dataset which is complex and time-consuming due to the high non-linearity in correlations.[5] Furthermore, using correlations will not always end with the expected results (similar operation and yield).[1]

With developments in high-performance computation capabilities, computational fluid dynamics (CFD) have become a good alternative to the dimensionless number-based design and scale-up. Detailed phenomenon

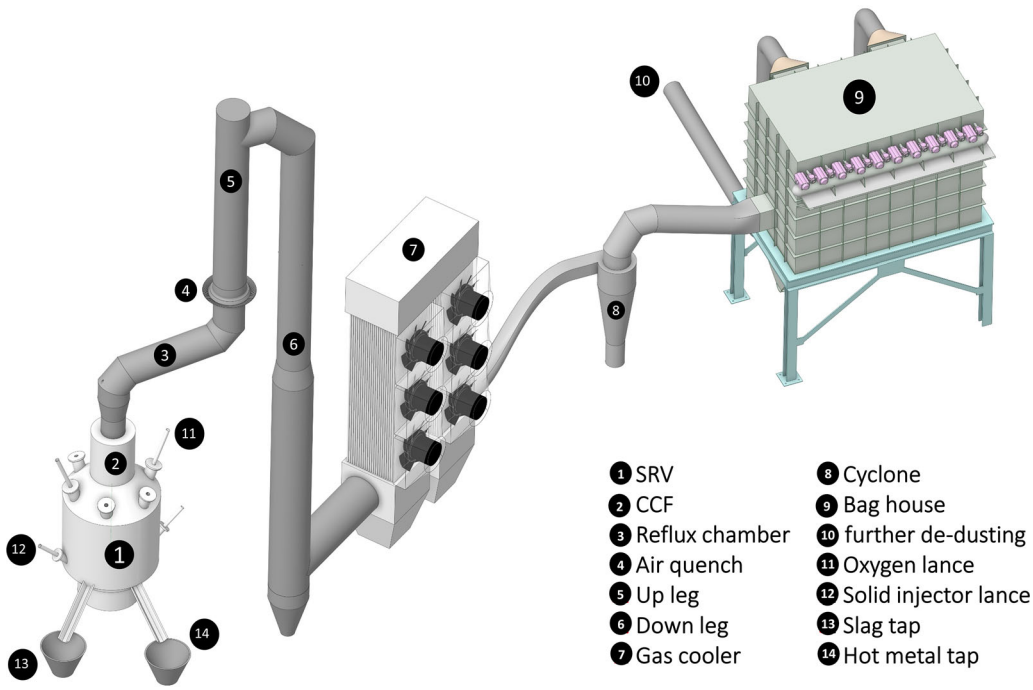

Fig. 1—Schematic overview of the HIsarna pilot plant main components.

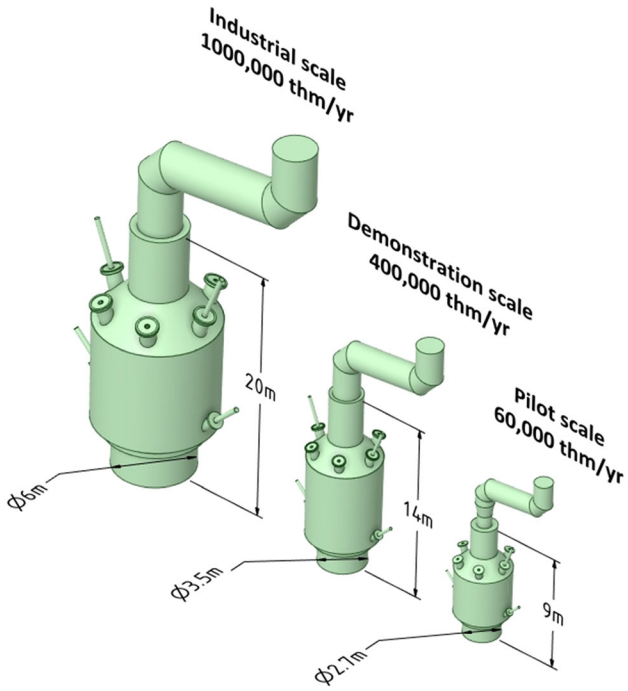

Fig. 2—Scaled up scheme of main reactor and reflux chamber for pilot, demo, and industrial scale.

can be implemented in CFD models with which the scale-up calculation can be performed much easier and more effective in comparison with the traditional ways.[1,5]

There are quite number of CFD-assisted scale-up studies in literatures for different processes such as fermentation,[6–8] coal combustion, gasification and burners,[9–12] bioreactors and bubble columns,[1,5,13–16] gas cleaning and upgrading,[17,18] spouted and fluidized beds,[11,19,20] and crystallization reactors.[21]

To mention few, Azuhata *et al.*[9] have performed a CFD-based analysis of a coal burner to scale up from laboratory to pilot scale with 25 times higher coal feed rate. They have developed and validated a base model using laboratory data and modeled the pilot cases to evaluate the performance and the gaseous composition profiles. According to derived results, for coal combustors, determining mixing times of oxidant with fuel is a major challenge in scale-up process.

In another study, Singh *et al.*[10] have used laboratory data of gas–solid vortex reactor to developed and use a CFD model for scale-up purpose. A geometrical optimization is performed by investigating the effect of length to diameter ratio on solid loading capacity and particle loss in the reactor.

Biglari *et al.*[12] have performed scale-up of a small-scale fluidized bed gasifier using both CFD and dimensionless numbers and reported accurate prediction of hydrodynamics and pressure drop using CFD models. Important design and operation parameters such as minimum fluidization velocity and solid velocity are accurately predicted and they have reported higher efficiency and robustness of CFD models compared to dimensionless numbers for scaling-up procedure.

Cui *et al.*[11] have performed CFD modeling of circulating fluidized bed (CFB) for laboratory, pilot, and industrial scale. Their main focus was on flow dynamics, angles of furnace, gas–solid flow interaction, combustion and heat transfer characteristics, and more importantly the effect of scale on gas emission and boiler efficiency. As the scale of the boiler is increased, lower emissions of CO, NOx, and SO_2 are predicted. On the other hand, carbon conversion and combustion efficiency are reduced for industry-scale boiler with lower thermal input.

Ali *et al.*[13] have investigated the role of CFD modeling for scaling up the sparger of a photo bioreactor. To develop their pilot scale CFD model, they have incorporated detailed algal growth kinetic to study and optimize the sparger parameters such as number and diameter of holes and gas flow rate. The final design and scale-up correlations are proposed based on the effect of studied parameters on generated bubble volume fraction, average light intensity, friction velocity, power input, and biomass concentration.

II. CASE STUDY

In this section, the case study of HIsarna off-gas system is described in details. For the pilot scale, a CFD mode is developed for the whole off-gas system. A special attention is paid to the correct modeling of the walls which has a different geometry in pilot and industrial scale. It is quite important to develop a general procedure to design and to correctly predict the necessary thermophysical properties of the wall which will be used as input for the CFD models. The same model is used for scaling up to the industrial scale of the reflux chamber section.

A. *Off-Gas System Components and Reflux Chamber*

In Figure 3, a schematic view of HIsarna off-gas system is depicted in details. It is divided into four parts namely "Reflux Chamber," "Air Quench," "Up Leg," and "Down Leg" with hot gas entering the reflux chamber which is right above the CCF. Oxygen is injected through a port to burn CO–H_2 mixture and carbon particles in the flue gas. Due to exothermic reactions, the temperature of the hot flue gas raises even higher. The gas then enters the air quench section where air is injected to rapidly quench the flue gas to reach an appropriate temperature for further cleaning and treatment process such as dust capturing and sulfur removal.

In special cases where further temperature reduction is required, a set of blast atomizer is activated to inject water (with nitrogen as carrier gas) to perform evaporative cooling. The flue gas ultimately enters the gas cooler from "Point D."

In current operation, the temperature is measured at points A, B, and D; however, the gas composition is available only at points A and D. These measurements are used for model validation.

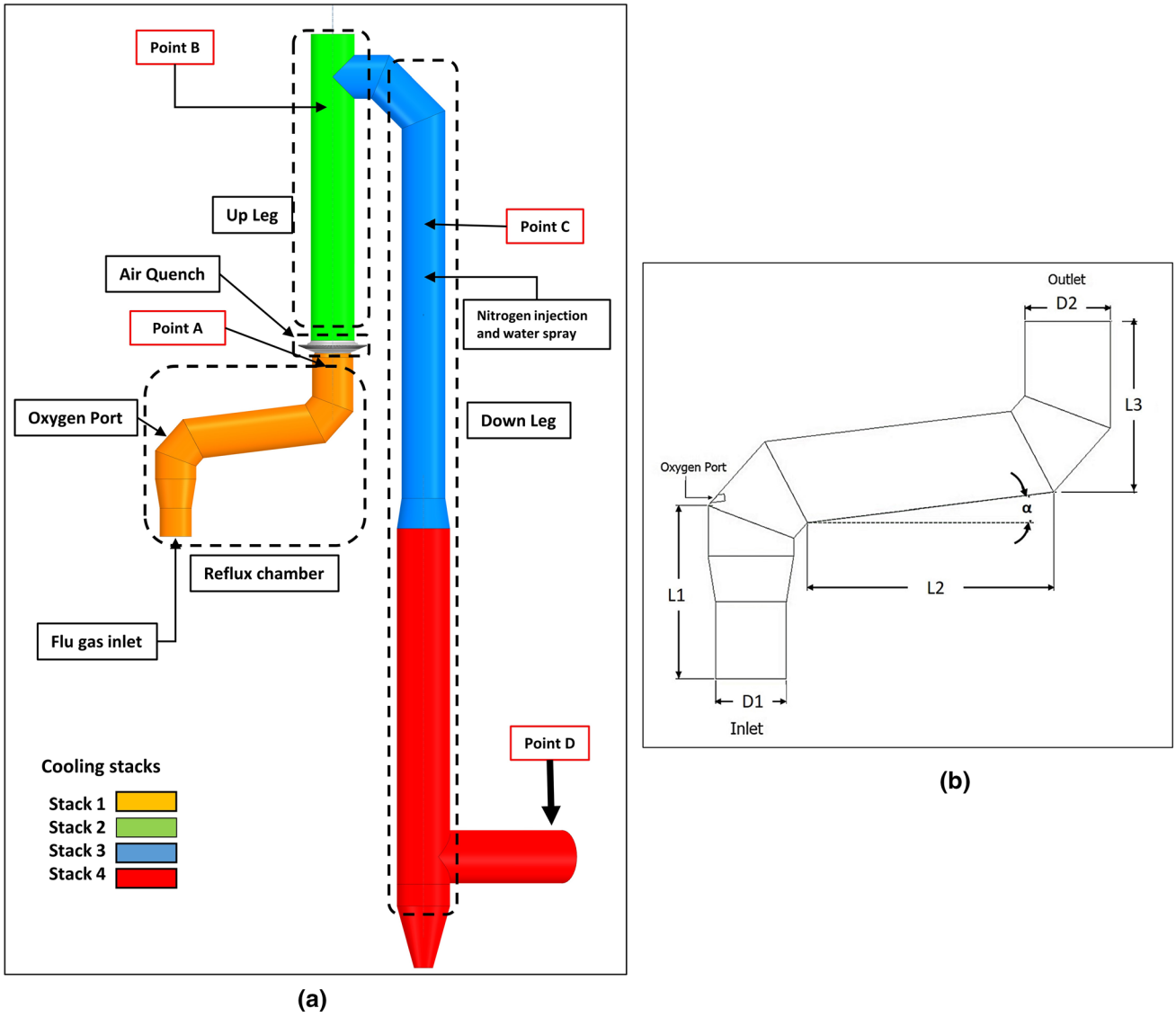

Fig. 3—(*a*) Pilot scale off-gas system components and data acquisition points (point A: reflux chamber outlet, Point B: end of up leg, Point C: 3 m above water quench atomizers, Point D: exit to gas cooler) and (*b*) reflux chamber dimensions (see Table VIII for the lables).

B. *Off-Gas System Walls*

The walls of the off-gas system are made of welded steel pipes in circular pattern forming a cooling jacket as shown in Figure 4(a). Cooling water is running through the pipes to maintain proper wall temperature during the operation. The cooling pipes are covered by a uniform layer of refractory material with a very low thermal conductivity to prevent the pipes from melting due to a very high temperature of the flue gas. Above the reflux chamber, the cooling pipes are bare and without refractory coating. Rows of anchors are placed on each cooling pipe inside the reflux chamber, to firmly hold refractory material as shown in Figure 4(a). The original average thickness of fresh refractory layer for pilot plant is 49.5 mm which is 1 cm above the anchor tips. In long-term operations, the thickness of refractory material is reduced due to erosions and thermal stresses. Along with this, the escaped molten iron ore particles from CCF create accretion and build up on some part of the refractory, making the behavior of the reflux chamber wall more complicated compared to the rest of the off-gas system.

Figure 4(b) shows the reflux chamber walls (used wall or non-fresh wall) near the oxygen lance during 2020 inspection. Based on the observations near the reflux chamber inlet where the temperature is the highest, the erosion is to a point that the tip of the anchors becomes visible. The averaged refractory thickness is determined to be between 32 and 38 mm with data obtained from laser measurement at different cross sections which are lower than the original fresh wall thickness (49.5 mm). The details of the measurements are not presented in this paper. This change in thickness must be take into account during CFD modeling as it determines the heat

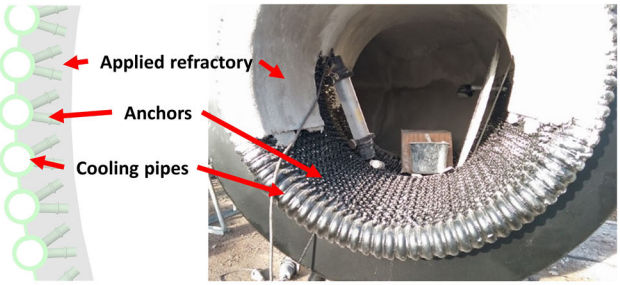

(a)

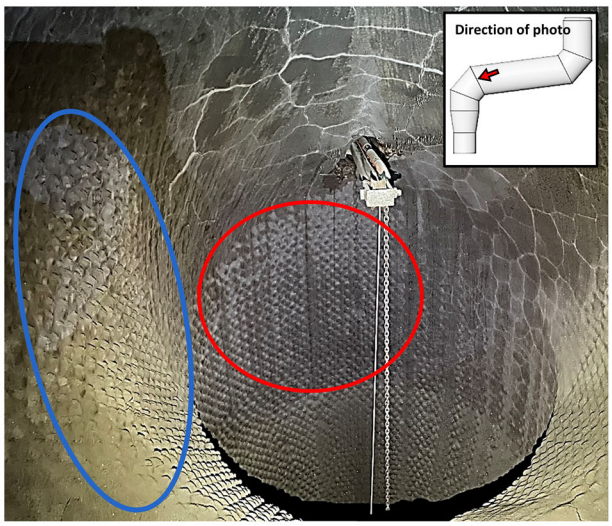

(b)

Fig. 4—(*a*) Reflux chamber cooling jacket and fresh refractory layer; (*b*) Reflux chamber refractory layer after operation (inspection 2021).

loss through the walls and predicted temperature profile and corresponding composition profiles. Considering inaccurate thickness and wall properties might lead to wrong temperature and composition profile predictions.

III. SCALE-UP PROCEDURE

The scale-up process in this study can be divided into following steps:

- A CFD model is developed for pilot scale by considering the whole off-gas geometry and implementing all possible phenomena and detailed wall modeling.
- The model is validated using measured temperature, heat loss, and composition at different points.
- Inlet condition for industrial scale is available from predictions of scaled up CCF model. Using the inlet condition, the oxygen required for full combustion of coal and CO–H_2 mixture is calculated
- The wall properties such as thermal conductivity, density, heat capacity, and thickness are determined *via* FEM analysis by considering proper cooling pipe diameter, anchor length, and refractory thickness
- The final geometry is proposed using the defined boundary conditions and the validated CFD model. The geometry then is modified to meet the hydrodynamic requirements.
- A sensitivity analysis is performed to make sure that the proposed design can meet the requirement for various operating conditions.

In following sections, all of the mentioned steps above will be discussed in details.

A. *CFD Modeling and Validation of Pilot Case*

Detailed discussion on governing equations, mesh, boundary conditions, and software settings for CFD model development of pilot scale off-gas system is presented in another study.[22] However, to make this research paper stand out independent and more comprehensive, a quick review of the model development and governing equations are mentioned in the followings. The same governing equations and solution procedure is applied for the industrial scale CFD models.

1. *Governing equations*

The main solved equations are listed in Table I. All of the equations, definitions, and constants are taken from Ansys Fluent Theory Guide.[23] To obtain pressure, velocity and density field continuity (1) and momentum (2) equations are solved first.

To include the effect of turbulent flow, Realizable k-ε Model is utilized and transport equations for k (3) and ε (4) are solved. As mentioned before, the inlet flue gas is at high temperature which creates a considerable temperature gradient with the cooling walls. In such systems with high flow temperature and/or with high temperature difference between gas flow and solid surfaces, the effective of radiative heat transfer cannot be ignored. Discrete ordinate model (6) is considered to include the effect of radiation in the source term of the energy Eq. (5) for correct prediction of heat fluxes and temperature profile. A composition-dependent absorption coefficient model, known as weighted-sum-of-gray-gases model (WSGGM), is used instead of constant absorption coefficients. We would like to refer readers to References 16 through 19 for more details on absorption coefficients for gray gases. Species transport Eq. (7) is solved to acquire composition distribution in the off-gas system. In reactive flow, the source term R_i is calculated based on the turbulence interaction models. In this study, eddy dissipation concept (EDC) model[4] is considered for source term calculations in species transport equation.

Particle behavior (for carbon and water liquid particles) is modeled using the discrete phase method (DPM) (8). Detailed kinetic mechanism proposed by Cuoci *et al.*[5] is used for CO–H_2 mixture combustion and carbon is combusted through the kinetic data and expressions proposed by Wen *et al.*[6] Liquid droplets evaporation is modeled using convection/diffusion submodel as written in Eq. (9).

Table I. Governing Equations and Sub-models for CFD Modeling of HIsarna Off-Gas System

Name		Main Equation
Continuity Equation	(1)	$\frac{\partial}{\partial t}(\rho)+\frac{\partial}{\partial x_i}(\rho\overline{u_i})=0$
Momentum Equation	(2)	$\frac{\partial}{\partial t}(\rho\overline{u_i})+\frac{\partial}{\partial x_j}(\rho\overline{u_iu_j})=-\frac{\partial p}{\partial x_i}+\frac{\partial}{\partial x_j}\left[\mu\left(\frac{\partial\overline{u_i}}{\partial x_j}+\frac{\partial\overline{u_j}}{\partial x_i}-\frac{2}{3}\delta_{ij}\frac{\partial\overline{u_l}}{\partial x_l}\right)\right]+\frac{\partial}{\partial x_j}\left(-\rho\overline{u_i'u_j'}\right)$
Turbulence Models		Realizable k-ε Model
		Equation for turbulent kinetic energy (k)
	(3)	$\frac{\partial}{\partial t}(\rho k)+\frac{\partial}{\partial x_i}(\rho k\overline{u_i})=\frac{\partial}{\partial x_j}\left[\left(\mu+\frac{\mu_t}{\sigma_k}\right)\frac{\partial k}{\partial x_j}\right]+G_k+G_b-\rho\varepsilon-Y_M+S_k$
		Equation for dissipation of turbulent kinetic energy (ε):
	(4)	$\frac{\partial}{\partial t}(\rho\varepsilon)+\frac{\partial}{\partial x_j}(\rho\varepsilon\overline{u_j})=\frac{\partial}{\partial x_j}\left[\left(\mu+\frac{\mu_t}{\sigma_\varepsilon}\right)\frac{\partial\varepsilon}{\partial x_j}\right]+\rho C_1S\varepsilon-\rho C_2\frac{\varepsilon^2}{k+\sqrt{\vartheta\varepsilon}}+C_{1\varepsilon}\frac{\varepsilon}{k}C_{3\varepsilon}G_b+S_\varepsilon$
Energy Equation	(5)	$\frac{\partial}{\partial t}(\rho E)+\nabla.(\overline{u}(\rho E+p))=\nabla.(k_{eff}\nabla T-\sum_j h_j\overrightarrow{J_j}+(\tau_{eff}.\overline{u}))+S_h$
Radiation Models		Discrete ordinate model (DOM)
	(6)	$\nabla\cdot(I(\vec{r},\vec{s})\vec{s})+(a+\sigma_s)I(\vec{r},\vec{s})=an^2\frac{\sigma T^4}{\pi}+\frac{\sigma_s}{4\pi}\int_0^{4\pi}I(\vec{r},\vec{s}')\phi(\vec{s},\vec{s}')d\Omega'$
Species Transport Equation	(7)	$\frac{\partial}{\partial t}(\rho Y_i)+\frac{\partial}{\partial x_i}(\rho\overline{U}Y_i)=-\nabla.\overrightarrow{J_i}+R_i+S_i$
Particle Force Balance Equation Discrete Phase Model	(8)	$m_p\frac{d\vec{u}_p}{dt}=m_p\frac{\vec{u}-\vec{u}_p}{\tau_r}+m_p\frac{\vec{g}(\rho_p-\rho)}{\rho_p}+\vec{F}$
Particle Evaporation Model	(9)	$\frac{dm_p}{dt}=k_cA_p\rho.Ln\left(1+\frac{Y_{i,s}-Y_{i,\infty}}{1-Y_{i,s}}\right)$
Carbon Particle Reaction Rate	(10)	$\overline{R_{char}}=\frac{dm_c}{dt}=-A_py_jR_{char,i}$
	(11)	$R_{char,i}=\frac{1}{\frac{1}{k_{diff,i}}+\frac{1}{k_{s,i}Y^2}+\frac{1}{k_{dash,i}}\left(\frac{1}{Y}-1\right)}\left(P_i-P_i^*\right)$
Conductive Heat Transfer Equation	(12)	$\frac{\partial}{\partial x}\left(k_{s_x}(T)\frac{\partial T}{\partial x}\right)+\frac{\partial}{\partial y}\left(k_{s_y}(T)\frac{\partial T}{\partial y}\right)+\frac{\partial}{\partial z}\left(k_{s_z}(T)\frac{\partial T}{\partial z}\right)+Q=\rho_s(T)cp_s(T)\frac{\partial T}{\partial t}$

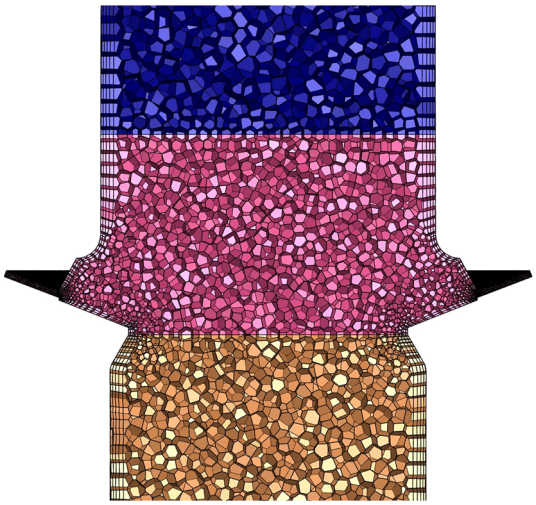

Fig. 5—Polyhedral cells used for CFD calculations—around the air quench region.

Finite element analysis is used to determine the thermal conductivity of the reflux chamber walls which can be considered as a composite with refractory material as matrix and anchors as fillers. The temperature field across the wall is calculated using the three-dimensional heat transport equation as stated Eq. (12). The utilized approach to calculate wall thermal conductivity is discussed in details in Section III–B–3.

2. *Geometry, mesh, and boundary conditions*

The pilot scale geometry of the whole off-gas system is shown in Figure 3. The geometry is meshed with polyhedral cells with cell size of 40, 30, and 50 mm for reflux chamber, air quench, and up/down leg region, respectively, with total of 2.4 million cells. A sampled meshed region of the off-gas system is shown in Figure 5. The same mesh size is used for the industrial case.

Table II summarizes the inlet condition for pilot scale CFD model which is taken from the plant measurements.

Table II. Inlet Boundary Conditions for CFD Model Setup

	Reflux Chamber	Air Quench	Oxygen Port	Nitrogen Ports	Water Spray
Inlet Temperature (K)	2086	293	293	293	293
Inlet Mass Flowrate (kg/s)	4.33	3.69	0.27	0.205	0.45
Composition – Average Mole Fraction					
CO	0.0261	0	0	0	0
CO_2	0.61	0.0003	0	0	0
H_2	0.002	0	0	0	0
O_2	0	0.21	0.995	0	0
N_2	0.166	0.78	0.005	1	0
H_2O	0.2	0.012	0	0	1
Post-Combustion Ratio (PCR)	96.63 pct	—	—	—	—

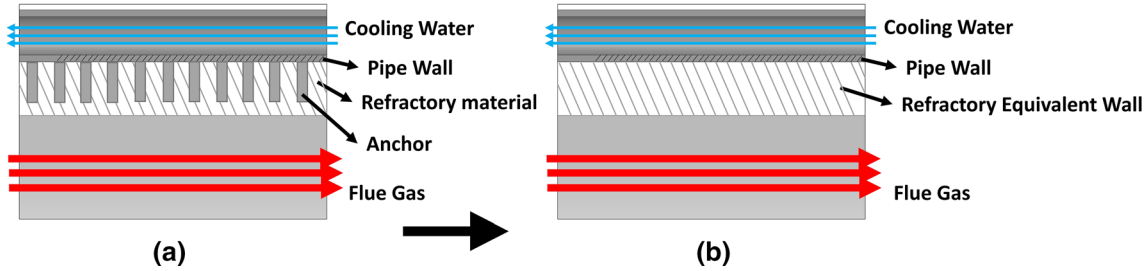

Fig. 6—Schematic representation of (*a*) detailed reflux chamber wall and (*b*) equivalent simplification.

For inlet boundary condition, a non-uniform species profiles are used (see Reference 22). In CCF section, the oxygen is injected *via* tilted injectors creating a swirl flow which is conveyed into the reflux chamber. To take into account the swirl effect, fixed swirl number of 0.6 is considered by defining radial and axial component for the inlet flow of the off-gas system. The flowrate of carbon particles is considered to be 0.0282 kg/s with uniform particle size of 120 μm. The diameter of water droplets is also considered uniform and equal to 90 μm and is injected with a velocity of 25 m/s.

Considering detailed geometry of the wall and including anchors (shown in Figure 4) will lead to a very fine mesh which in turn increases the computational cost. So in this study, the walls are not directly resolved and are modeled using "shell conduction" approach. In this approach, the wall details and thickness are not included in the geometry and the solver automatically grows a layer of prism or hex cells for the wall and conduction heat transfer equation is solved in all directions for the virtual cells. It is possible to consider different layers for the walls with specified thickness and thermophysical properties. Based on the assigned properties, appropriate thermal resistance across the wall thicknesses is imposed and wall conduction is taken into account.

As mentioned before, the reflux chamber walls are made of pipes with anchors (steel material) and a refractory layer applied on top of them [Figure 6(a)]. Above the reflux chamber, the walls are only made of bare steel pipes.

To obtain the properties of different wall layers for shell conduction modeling, the wall is simplified as shown in Figure 6(b). The first layer is indeed an equivalent wall representing pure refractory with embedded anchors. The second layer represents the cooling pipe wall thickness (5 mm thickness) with thermal and physical properties of the steel.

As discussed in brief, the properties of equivalent wall are calculated by considering it as a composite wall of matrix (refractory material) and fillers (anchors) through detailed geometry and FEM analysis. The equivalent wall properties depend on refractory and steel anchors properties and also the thickness of the refractory layer. According to the plant inspections and FEM calculations, the effective (average) refractory thickness is determined to be 37 mm for current plant data. This thickness is lower than the original refractory thickness of 49.5 mm which was applied during the construction. More detailed discussion on FEM analysis can be found in Section III–B–3 and another study by the same authors.[24] The properties of the pure refractory material (Calde Stix 151), steel (P235GH-TC1), and refractory equivalent wall which is obtained based on the FEM analysis are reported in Table III.

The outer layer of the pipe wall is considered to be in touch with cooling water (pressure: 1 bar). The heat transfer coefficients of water side are calculated for each cooling stack (shown in Figure 3) according to Pak and Cho relation.[25] The average temperature and heat transfer coefficient are assigned as follows: stack 1: 314 K and 5000 w/m^2-K; stack 2 and 3: 307 K and 4500 w/m^2-K; stack 4: 314.5 and 4000 w/m^2-K.

3. *Model validation*

Figure 7 shows the predicted temperature and compositions profile and as can be seen, the predictions are in fair agreement with the measured data.

Table III. Material Properties for FEM and CFD Analysis

Material	*Density* [Kg/ m^3]	Thermal Conductivity [W/m. K]	Heat Capacity [J/kg. K]	Thickness [mm]
Pure Refractory (Calde Stix 151)	2200	$k = \begin{cases} -0.0099 \times T[\mathrm{K}] + 59.7019273 \le T \le 370 \\ -0.0425 \times T[\mathrm{K}] + 71.7876370 < T \le 673 \end{cases}$	900	—
Steel (P235GH-TC1)	7850	$k = \begin{cases} 0.00025 \times T[\mathrm{K}] + 0.801751073 \le T \le 1273 \\ 0.0007 \times T[\mathrm{K}] + 0.22891273 < T \le 2273 \end{cases}$	461	5
Refractory Equivalent Wall*	3010	3.65	836	37

*For pilot scale case.

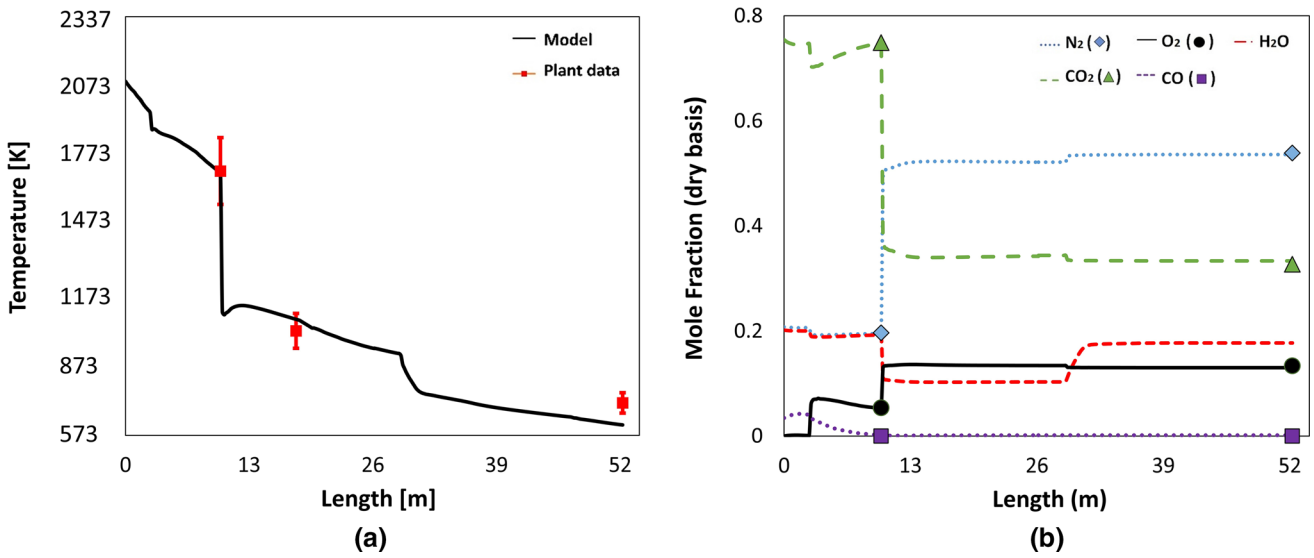

Fig. 7—(*a*) Predicted temperature and (*b*) composition profile *vs* plant measurements.

Table IV. Inlet Condition for Pilot and Industrial Scale

	Pilot	Industrial
Operating Condition		
Temperature [K]	2086.15	1891
Flue Gas Mass Flow [kg/s]	4.326	65.63
Carbon Mass Flow [kg/s]	0.0283	0.082
Carbon Particle Diameter [μm]	120	120
Inlet Diameter [m]	3.15	1.15
Operating Pressure [Pa]	100,925	181,297
Gas Composition		
CO	0.0261	0.157
CO_2	0.6065	0.503
H_2	0.002	0.0165
O_2	0	0
N_2	0.166	0.103
H_2O	0.1995	0.22
Sum	1.0001	0.9995
PCR	96.63 pct	80.65 pct

Table V. Cooling Water Operating Condition for Both Scales

Parameter	Pilot	Industrial
Temperature [K]	313 (40 °C)	473 (200 °C)
Pressure [bar]	1	18
Density [kg/m^3]	992	860
Viscosity [Pa. s]	6.53×10^{-4}	1.37×10^{-4}
Heat Capacity [J/kg. K]	4183	4500
Thermal Conductivity [W/m. K]	0.629	0.657
Velocity [m/s]	1	1
Pipe Diameter [m]	0.028	0.08
Re	42,562	502,189
Pr	4.34	0.938
Nu	232	836
h [W/m^2. K]	5,000	6,800

The calculated heat loss through the walls in MW is 3.92 (measured: 3.9; error: 0.5 pct), 4.85 (measured: 5.4; error: 10 pct) and 8.7 (measured: 8.7; error: 6.5 pct) for reflux chamber, rest of the off-gas, and the whole off-gas system, respectively.

The developed model is used to investigate different parameters in pilot scale and the results are discussed in details in other studies.[22,26] The same model will be used to design the industrial scale reflux chamber.

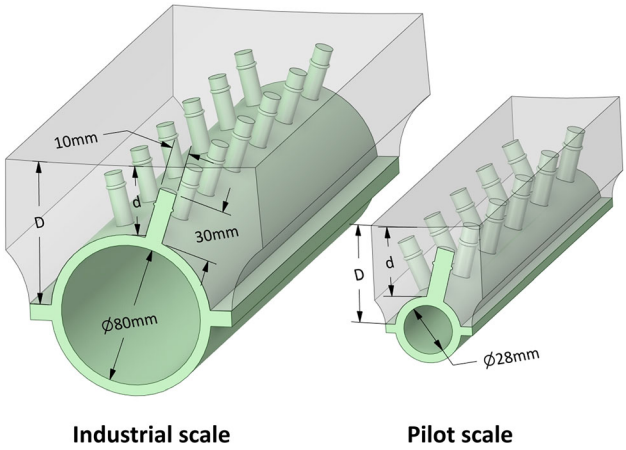

Fig. 8—Cooling pipe, anchors, and refractory wall depiction for pilot and industrial scale.

B. *Industrial Scale Modeling*

1. *Inlet boundary condition*

Table IV shows the inlet condition for pilot and industrial scale. Since there are no measurements available, the industrial inlet conditions are taken from the predicted outlet condition of the available CFD models for industrial scale CCF. The detail of CCF modeling is not mentioned in this paper. The operating pressure for industrial case is higher to avoid extremely large geometries.

2. *Oxygen injection calculations*

Using the available inlet conditions, the necessary stoichiometric oxygen to fully burn the unwanted species (CO–H_2–Carbon mixture) can be easily calculated by considering the following global reactions:

$$H_2 + 0.5O_2 \rightarrow H_2O \quad [13]$$

$$CO + 0.5O_2 \rightarrow CO_2 \quad [14]$$

$$C + O_2 \rightarrow CO_2 \quad [15]$$

For industrial case, a stoichiometric oxygen would be 5.7 kg/s (0.11 kg/s for pilot scale). An excess ratio of 4 is used for final oxygen injection flowrate similar to the pilot scale. Considering this access ratio, oxygen

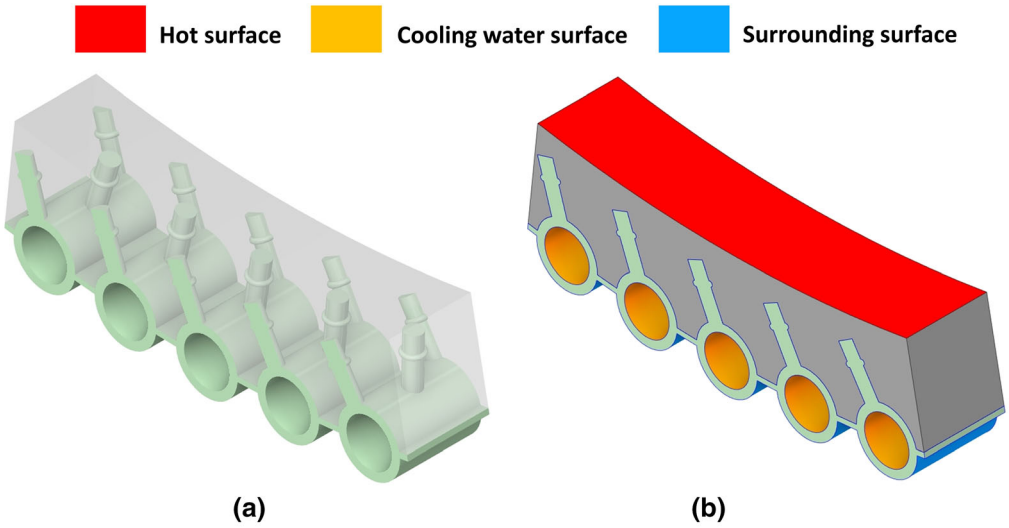

	Pilot	Industrial
Hot surface	T:1673 K, h: 200 W/m^2. K	T:1673 K, h: 200 W/ m^2. K
Cooling water surface	T:314 K, h: 5000 W/ m^2. K	T:473 K, h: 6800 W/ m^2. K
Surrounding surface	T:293 K, h: 50 W/ m^2. K	T:293 K, h: 50 W/ m^2. K

Fig. 9—(*a*) Unit cell geometry and (*b*) thermal boundary conditions for FEM analysis of unit cell for pilot scale (Color figure online).

Table VI. FEM Results for Pilot and Industrial Scale

d [mm]	25*	30	35	40	45	50
Industrial Scale						
HF (kW/m^2)	66.3	45.7	38.4	34.1	30	26.9
T_c [K]	482.5	480.78	479.62	479	478	477.5
T_h [K]	1402.2	1449.8	1481.6	1503	1523.2	1543
d_{eff} [mm]	46	51	56	61	66	71
k_{eff} [W/m. K]	3.31	2.4	2.15	2.1	1.9	1.79
ρ_{eff} [kg/m^3]	2648	2600	2562	2533	2503	2471
Cp_{eff} [J/kg. K]	865	869	872	874	876	879
Pilot scale						
HF (kW/m^2)	115	72.5	57.3	48.3	42	37.1
T_c [K]	332.6	328.66	325.5	323.5	322	321
T_h [K]	1257.64	1322.6	1386.5	1430.4	1462.5	1487
d_{eff} [mm]	34.5	39.5	44.5	49.5	54.5	59.5
k_{eff} [W/m. K]	4.29	2.88	2.4	2.16	2	1.89
ρ_{eff} [kg/m3]	3251	3136	3044	2970	2907	2855
Cp_{eff} [J/kg. K]	818	827	834	840	845	849

*Bare anchors.

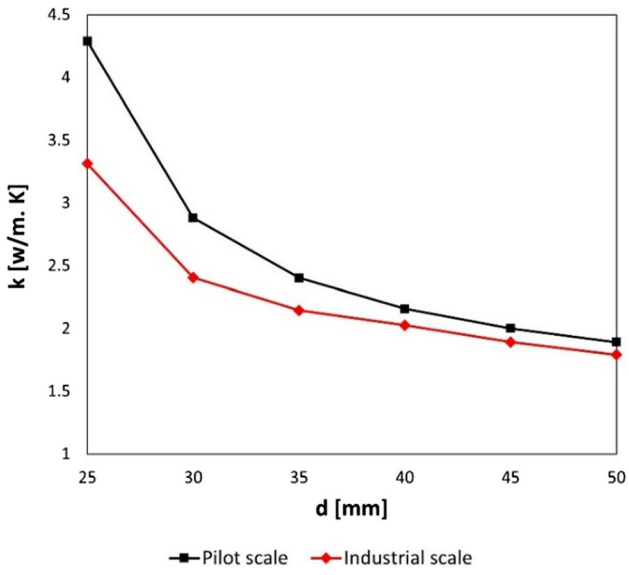

Fig. 10—Effective thermal conductivity of equivalent wall with respect to refractory layer thickness for pilot and industrial scale.

flowrate of 28.5 kg/s is calculated for the industrial scale. This value is used to develop the base model and afterward is optimized with a step-wise oxygen reduction to see the effect on the unwanted species removal inside the reflux chamber.

3. *Wall design*

For industrial scale, the cooling pipes that make up the cooling jacket have an inner dimeter (ID) of 80 mm and pipe wall thickness of 6 mm which is larger than that of pilot scale (ID: 28 mm, thickness 5 mm). In pilot scale, the cooling water is at atmospheric pressure with an average temperature of 313 K (40 °C), while pressurized water will be used for industrial scale due to much higher heat losses to the cooling circuit. The cooling water pressure is kept at 18 bar with an average temperature of 473 K (200 °C). This will change the properties of water and, accordingly, the convective heat transfer coefficient which determines the heat pickup capacity by the water. The thermophysical properties of water are obtained based on the equation of state and relations proposed by Wagner *et al.*[27] and Huber *et al.*[28,29] which can be easily accessed and calculated through NIST online calculator[30] for different temperature and pressure. Heat transfer coefficients of cooling water are calculated according to Pak and Cho relation[25] and reported in Table V for both scales.

The other important parameter is determination of effective properties of the equivalent wall discussed in Section III–B–2 and depicted in Figure 6. From the study of several parameters and conditions, the thermal conductivity has been found to be the driving physical parameter in thermal exchanges.[31] So it is quite crucial to obtain a proper values for thermal conductivities of the equivalent wall. Figure 8 shows the schematic view of pipe, anchors, and refractory wall with their respective dimensions for pilot and industrial scale.

The anchor dimension and geometry are considered to be the same for both scales. The wall thickness are represented with two variables: tip thickness ("*d*"), which refers to the wall thickness from the anchor base, and base thickness "*D*," which is the thickness from the middle of the cooling pipe. The tip thickness is the same for both pilot and industrial case. However, the base thickness is thicker for the industrial case since more refractory material is required to cover the cooling pipes. For FEM analysis, a symmetrical unit cell with surface thermal boundary conditions depicted in Figure 9 is used.

From FEM thermal analysis, it is possible to determine the heat flux through the unit cell and average temperature of the surfaces. The effective thermal conductivity of equivalent wall is calculated as follows:

Table VII. Summary of Boundary Conditions for Industrial Scale Base Model

Inlet Conditions	Reported in Table IV
Oxygen Injection [kg/s]	28.5
Wall layer properties	
First Layer (Equivalent wall)	
Effective Wall Thickness [mm]	61 (d = 40)
Effective Thermal Conductivity [W/m K]	2.1
Effective Density [kg/m^3]	2533
Effective heat capacity [J/kg K]	874
Second Layer (Steel Pipe Wall)	
Wall Thickness [mm]	6
Thermal Conductivity [W/m K]	$k = \begin{cases} 0.00025 \times T[\mathrm{K}] + 0.801751073 \leq T \leq 1273 \\ 0.0007 \times T[\mathrm{K}] + 0.22891273 < T \leq 2273 \end{cases}$
Density [kg/m^3]	7850
Heat Capacity [J/kg K]	461
Cooling Water Properties	
Heat Transfer Coefficient [W/m^2. K]	6800
Average Temperature [K]	473

Table VIII. Pilot and Final Industrial Scale Dimension (see Fig. 3b for Labels)

Dimension	Pilot	Industrial
D1 [m]	1.15	3.15
D2 [m]	1.39	3.15
L1 [m]	2.82	4
L2 [m]	4	9.5
L3 [m]	2.8	6.85
α	7°	7°
Oxygen Port Diameter [m]	0.03	0.14
Number of Oxygen Injector	1	4
Inner Wall Surface Area [m^2]	42	208.5

$$k_{eff} = \frac{HF}{T_h - T_c} . d_{eff} \quad [16]$$

d_{eff} is the average thickness of the refractory which is equal to $\frac{d+D}{2}$. In this calculation, the thickness of the cooling pipe is not included in d_{eff} and is directly modeled in CFD (second layer in shell conduction approach). Effective densities and heat capacities of the equivalent wall are calculated using mixing law and based on the anchor and refractory mass fractions as follows:

$$\rho_{eff} = m_{anchor}\rho_{anchor} + m_{refractory}\rho_{refractory}$$

$$cp_{eff} = m_{anchor}cp_{anchor} + +m_{refractory}cp_{refractory} \quad [17]$$

The obtained values from FEM analysis and effective properties for different tip thickness (“*d*”) are reported in Table VI and effective thermal conductivity is plotted in Figure 10 for both scales and for different “*d*” values. It is worth mentioning that in case with d = 25 mm, the thickness of the refractory material is lower than the length of the anchors and their tips become visible.

As it can be seen, the effective thermal conductivity for equivalent wall of the industrial scale is lower than the pilot case for the same “*d*” value. The reason is smaller anchor size with respect to pipe dimeter and also higher volume fraction of refractory material in industrial scale wall.

This is an important finding and it reveals that the same wall boundary condition cannot be used for different scales and wall properties must be calculated through detailed analysis and by considering detailed geometry and correct thermal boundary conditions.

4. *Industrial scale model summary*

The summary of boundary conditions for industrial scale “base model” is reported in Table VII. The same mesh size is used to create computational grid for the scaled up reflux chamber which generates a computational grid with 2.2 million cells (450 thousand cells for pilot scale reflux chamber).

All included models such as radiation, turbulence, chemistry, and kinetics are the same as discussed in Section III–A–1.

The simulations are steady state with second-order upwind scheme to discretize the conservation equations. All simulations are performed for 2000 iterations to achieve a convergence criterion of 10^{-4} for the relative error between two successive iterations.

IV. RESULTS AND DISCUSSION

A. *Geometry and Oxygen Injectors*

In pilot scale, the oxygen is injected through a single injector with a diameter of 3 cm. This diameter is suitable enough to reach a tip velocity of 200 m/s. It is desired to keep the injection Mach number lower than 0.5 for the industrial scale. The initial diameter for a single injector is determined to be 27.5 cm to keep the Mach number low. However, this dimeter is quite large

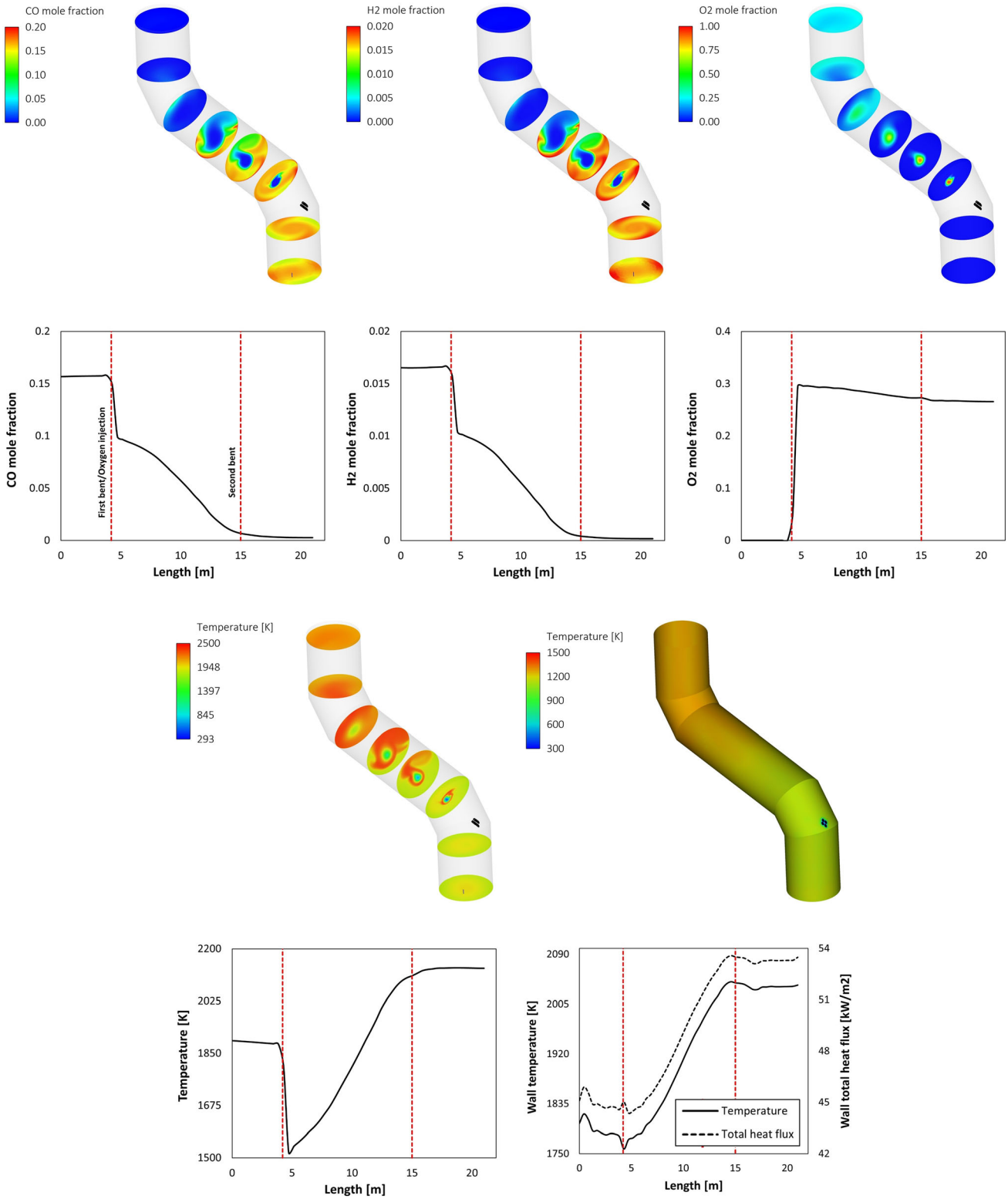

Fig. 11—Temperature and composition contours and corresponding profiles below each contour (Color figure online).

for a single injector and might be difficult to install and maintain during the operation. So for industrial scale, the same oxygen amount is injected by higher number of smaller injectors. Based on the hydrodynamic analysis, 4 injectors with dimeter of 14 cm is considered for final design. Using the same hydrodynamic analysis, the initial horizontal length (L2 dimension in Figure 3) of the reflux chamber is varied to determine the best length. The determination is based on the oxygen and flue gas streamlines to have minimum recirculation inside the

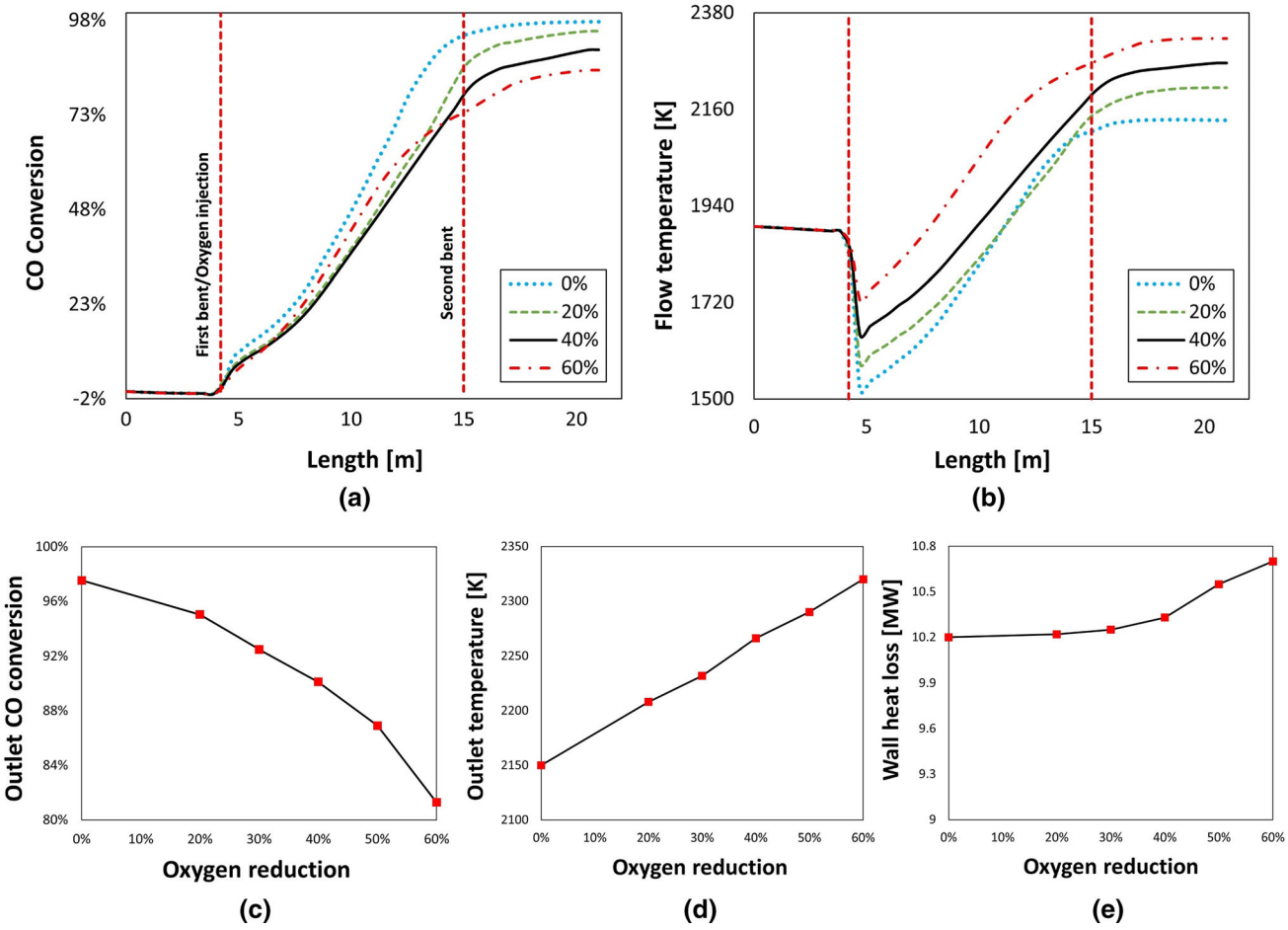

Fig. 12—Effect of oxygen reduction on CO conversion and temperature profile along and at the outlet of the reflux chamber; (*a*) CO conversion; (*b*) flow temperature; (*c*) reflux chamber outlet CO conversion; (*d*) reflux chamber outlet temperature; (*e*) reflux chamber wall heat loss.

reflux chamber and also avoiding oxygen jet to hit the walls. The final dimension for industrial scale is reported in Table VIII with labels shown in Figure 3.

B. *Base Model*

Figure 11 shows the temperature, composition contour, and profile along the reflux chamber length. The profiles are plotted as average value over a cross section, swept along centerline of the system (length).

The amount of CO and H_2 is slightly increased before the oxygen injection point (length: 4.4 m). This is mainly due the CO production from carbon gasification with H_2O-CO_2 mixture and also CO_2–H_2O dissociation into CO and H_2. Over the same length, the temperature decreases with a constant pace mainly due to heat losses through the wall, endothermic dissociation of CO_2 and H_2O, and endothermic gasification of carbon with H_2O-CO_2 mixture. Then, there is a sharp increase in oxygen concentration where oxygen is injected in the reflux chamber with a severe drop in local temperature. Due to the combustion of CO and H_2, oxygen content is reduced and temperature is increased and becomes constant after the second bent. The wall temperature is almost constant up to the oxygen injection zone and is

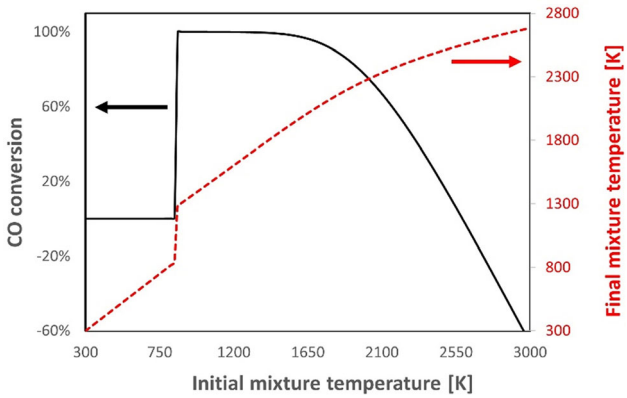

Fig. 13—Effect of temperature on CO conversion of a batch model analysis.

increased without noticeable drop. This is because the oxygen is injected in the centerline of the reflux chamber and it is not uniformly spread in the cross sections. This leads to much lower local flow temperature in the middle of the cross sections and higher wall temperature (a near wall) around the oxygen injection zone. The total heat

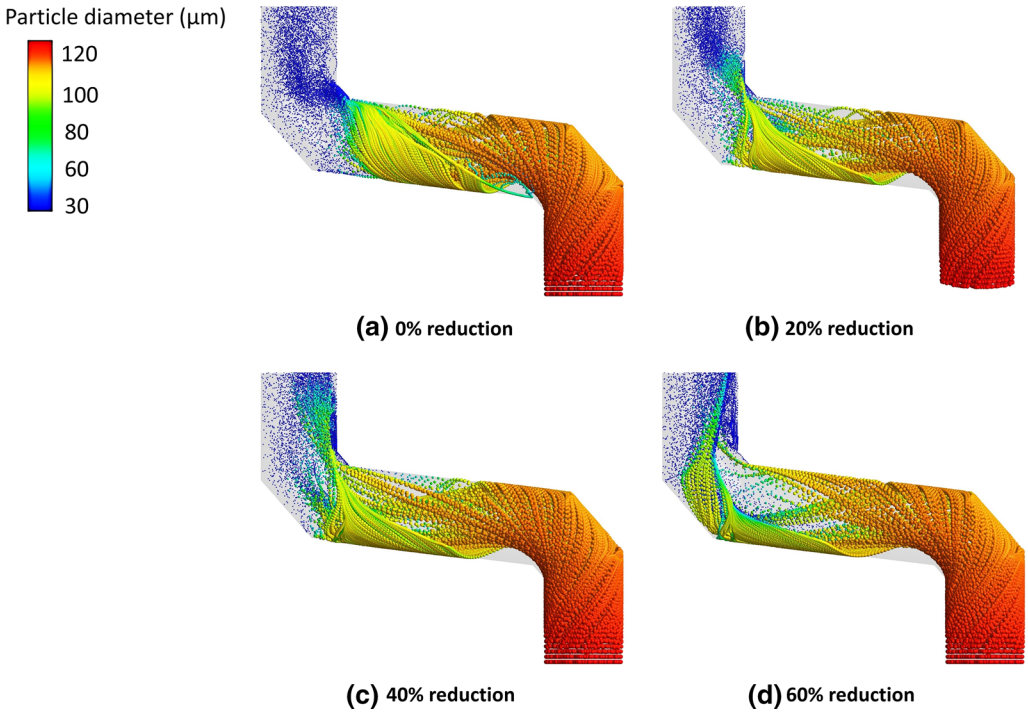

Fig. 14—Carbon particle track for different oxygen reduction cases; (*a*) 0 pct reduction; (*b*) 20 pct reduction; (*c*) 40 pct reduction; (*d*) 60 pct reduction (Color figure online).

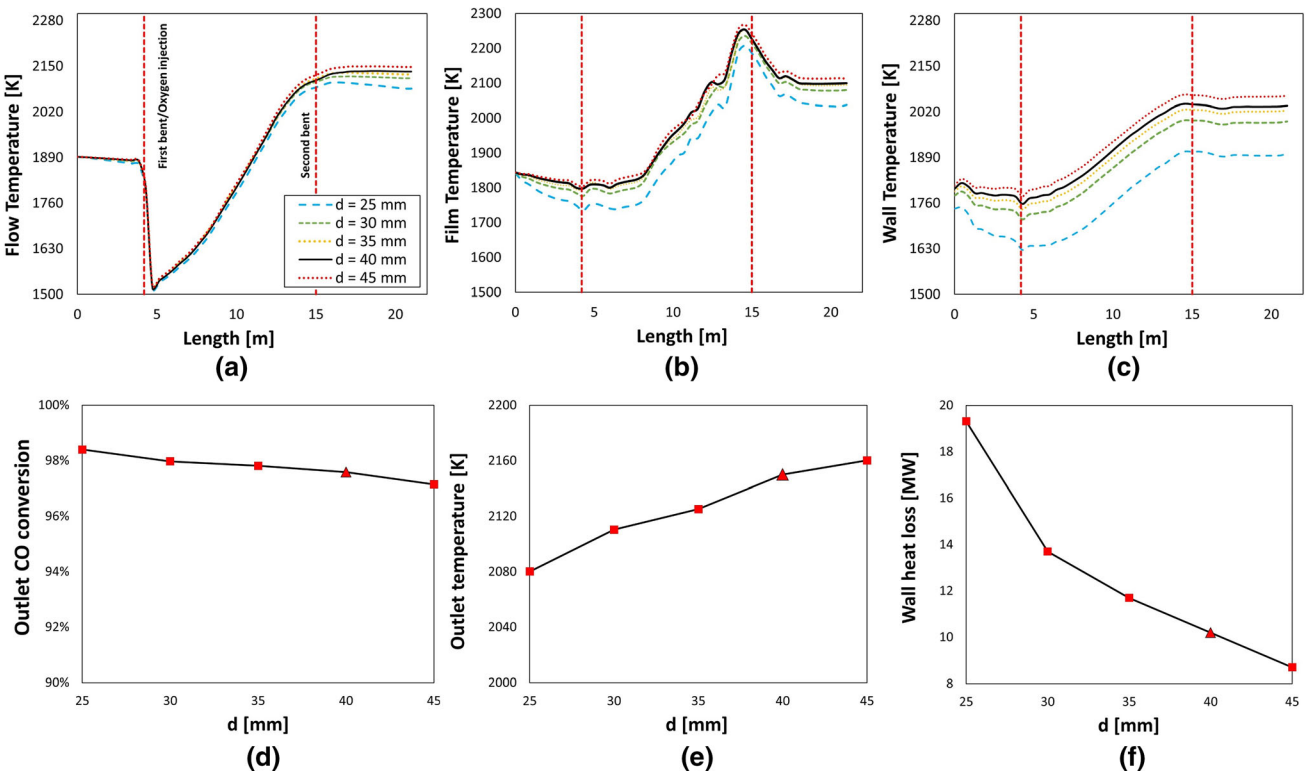

Fig. 15—Effect of wall thickness reduction on CO conversion and temperature profile along and at the outlet of the reflux chamber; (*a*) flow temperature; (*b*) film temperature; (*c*) reflux chamber wall temperature; (*d*) reflux chamber outlet CO conversion; (*e*) reflux chamber outlet temperature; (*f*) reflux chamber wall heat loss.

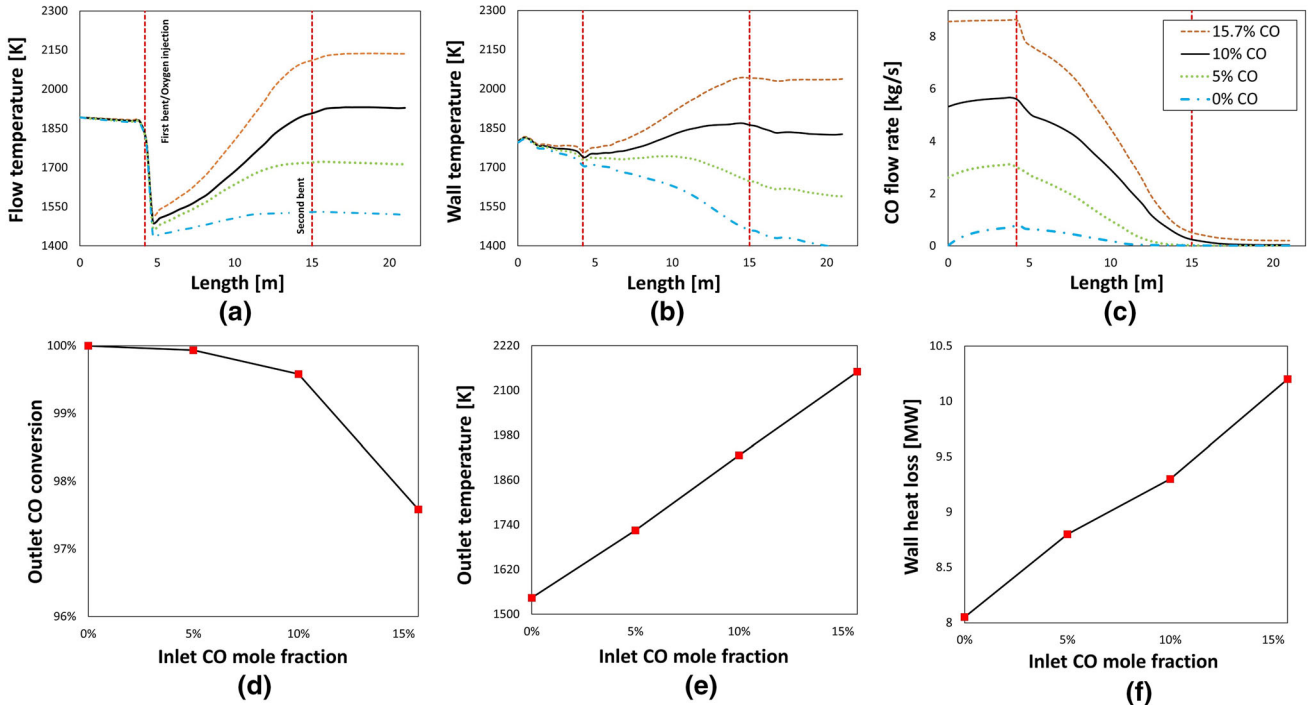

Fig. 16—Effect of inlet CO content on CO conversion and temperature profile along and at the outlet of the reflux chamber; (*a*) flow temperature; (*b*) reflux chamber wall temperature; (*c*) CO flow rate; (*d*) reflux chamber outlet CO conversion; (*e*) reflux chamber outlet temperature; (*f*) reflux chamber wall heat loss.

flux follows the same exact trend as wall temperature and is sharply increased at the combustion region between the two bent. With the current design and operating conditions, full combustion of CO–H_2–carbon mixture is achieved in a short length of the reflux chamber.

C. *Effect of Oxygen Injection and Optimization of Post-combustion*

The calculated oxygen flowrate of 28.5 kg/s is based on the access ratio of 4, similar to pilot case, to assure full combustion of all unwanted species. A set of simulations are performed to investigate the effect of the oxygen flowrate reduction (20 pct reduction intervals) on CO–H_2–carbon mixture combustion. Figure 12 shows the effect of this reduction on CO conversion and temperature profile inside the reflux chamber. Conversion of unwanted species is calculated as:

$$conversion = \frac{\dot{m}_{(inlet)} - \dot{m}_{(atanylocation)}}{\dot{m}_{(inlet)}} \qquad [18]$$

As can be seen, the profiles follow a similar trend as discussed before. Oxygen reduction has a negative effect on CO conversion for two main reasons. Firstly, reducing oxygen will reduce the amount and penetration of oxygen inside the flue gas which in turn reduces the conversion of unwanted species. Secondly, since oxygen is injected at room temperature, it has considerable local cooling effect thus reducing the injection, which increases the flu gas temperature. As can be seen, the temperature at the injected point is considerably reduced at higher oxygen injection flowrates. Increasing temperature has a negative effect on CO–H_2 combustion. To investigate this effect in more details, a Chemkin® analysis is performed using the same kinetic data used in CFD models.

A mixture with the same components reported in Table IV (industrial scale inlet) is considered for a batch reactor model analysis at different initial mixture temperature. Figure 13 shows CO conversion and final temperature of the mixture for different initial temperature. As can be seen, the conversion is zero below 850 K which is auto-ignition point of the specified mixture. By increasing the initial temperature, both conversion and final temperature are increased; however, further increase in initial and final temperature will lead to a lower CO conversion as CO_2 start to dissociate into CO mainly through thermal dissociation and reverse water gas shift reactions. As it is evident, after a certain temperature, negative conversion is predicted which means net production of CO inside the mixture.

With this analysis, it is clear now reducing the oxygen increase the flue gas temperature which in turn can reduce the CO conversion. So increase in temperature is not always beneficial for CO–H_2 removal and there is an optimum temperature range for full conversion of those species.

Figure 14 shows the carbon particle tracks colored by particle diameter for different oxygen reduction cases. Reducing the injection can reduce the carbon conversion inside the reflux chamber. However, for the current design, even for highest considered oxygen reduction, negligible amount of carbon emission is predicted. On the other hand, the full carbon conversion inside the

reflux chamber for pilot scale could not be achieved (maximum: 50 to 70 pct) even for highest oxygen injection excess ratio. The reason is less available length and volume in pilot geometry which provides less residence time for carbon particles inside the reflux chamber to fully react with oxidants.

Oxygen reduction has a negligible effect on the heat loss through the wall and it is slightly increased by reducing the oxygen injection which is linked to the flow temperature increase.

According to pilot plant data, emissions from reflux chamber can be still removed in air quench section of the off-gas (above the reflux chamber) where the temperature is still high. However, the aim is to achieve full removal of unwanted species inside the reflux chamber as there is a risk of temperature reduction below the auto-ignition point of the gaseous mixture above the air quench section. Moreover, since there will be an integrated heat exchanger to recover het from the whole off-gas system, it is desired to recover heat mostly from high-temperature zones like reflux chamber. So full combustion of the CO–H_2 and carbon particles inside the reflux chamber is beneficial to heat recovery efficiency since the thermal content of the flue gas is drastically reduced above the reflux chamber due to quenching by air.

So reducing oxygen injection is possible, but it should be in a quantity that the unwanted species (CO and carbon) are still combusted at a higher temperature than the auto-ignition point and avoiding a emission of CO into the off-gas sections where the temperature is lower. In conclusion, the amount of reduced oxygen depends on the environmental regulations and the amount of permitted CO emission. A full scaled up off-gas system modeling, including all sections, is required for a better analysis.

D. *Effect of Wall Thickness*

The base model is set up considering fresh refractory tip thickness similar to the pilot scale (d = 40 mm). As discussed in Section II–A, the refractory layer thickness is thinning due to the harsh condition (chemical and thermal stresses) inside the reflux chamber. From pilot plant measured data and modeling, the wall condition inside the reflux chamber determines the temperature and composition profiles throughout the whole off-gas system. It also has a direct effect on the off-gas system heat recovery and upstream equipment performance.

A set of simulations is performed to study the effect of gradual reduction in refractory layer thickness to see the response of the system. Along with thickness reduction, effective thermal and physical properties of the equivalent wall (first layer used in the shell conduction modeling) are also changed as reported in Table VI for industrial case. Figure 15 shows the temperature and composition profile for different refractory tip thickness.

As illustrated, by reducing the wall thickness, a major increase in heat loss through the wall is predicted [Figure 15(f)]. The increase in heat loss is more pronounced for d = 25 mm where the tip of anchors becomes visible and more heat is conducted through the tips into the cooling pipes. The average flow temperature [Figure 15(a)] is almost similar for all studied wall thicknesses but reduces at the outlet for the thinner walls. However, a noticeable reduction in temperature is observed for film (flow temperature in vicinity of the wall) and wall temperature once the wall thickness is reduced. This is related to the higher thermal conductivity and heat losses through thinner walls. Since the wall thickness has a minor effect on the mean flow temperature (especially in the middle of the flow), no major difference in CO conversion is predicted. However, the conversion is slightly higher for thinner walls which can be related to a lower temperature after the second bent. As discussed in Section IV–C and illustrated in Figure 13, lowering the flow temperature can increase CO conversion. Nevertheless, it is required to renew the refractory layer once thermal losses and emissions from the off-gas system are reaching a defined critical threshold.

E. *Effect of CO at the Inlet*

The HIsarna process has a transient nature during which parameters are changed to maintain a steady performance and production. For instance, flue gas flow rate, temperature, carbon flow rate, and gaseous composition entering the off-gas system are fluctuating. From pilot scale measurements, the CO content of flue gas can vary from 0 to 15 pct at its peak and the same trend is predicted for industrial scale. According to the measurements and prediction from CFD model of pilot scale, since CO content of flue gas acts as a fuel for combustion, its content can drastically change the behavior of the flow and therefore the performance of the off-gas system components. A set of simulation is performed to investigate the effect of CO content on the performance reflux chamber and results are reported in Figure 16. As can be seen, depending on the content of CO, the trends of the previously discussed results are drastically changed as CO is the main heat-generating source.

The amount of CO is increasing in the flue gas before hitting the oxygen injection area. This increase is more pronounced for lower inlet CO content. The reason is lower partial pressure of CO in flue gas which is favorable for reverse reactions leading to CO production at high temperature. By increasing inlet CO content, the partial pressure of CO is increased and forward reactions are proceeded with lower net production of CO. Also higher CO content is detrimental to carbon conversion and reduces the CO production from carbon gasification reactions.

For 0 pct CO content, the flow temperature during and after oxygen injection is relatively constant and the wall temperature is continually reduced. Higher CO content means higher fuel for combustion and therefore higher flow and wall temperature and also higher heat losses through the wall is expected.

It is important to mention that 0 pct CO content inside the off-gas system at the inlet of reflux chamber is unlikely to happen according to pilot plant measured data. The only condition that makes this scenario

possible is presence of oxygen at the inlet flue gas which is not the case here. Nevertheless, it still worth considering this possibility to have a better understanding of the effect of gaseous composition on reflux chamber performance and flow behavior.

V. CONCLUSIONS

A CFD-assisted scale-up design for reflux chamber of HIsarna off-gas system is performed for a pilot to industrial transition. Despite traditional methods, CFD analysis is a great tool to include even smallest details in system geometry and calculations.

A validated CFD model is used for hydrodynamic analysis of the scaled up case to determine the initial geometry and oxygen injection flow rate and to achieve full combustion of unwanted species (CO–H_2–carbon mixture).

The effect of oxygen injection, refractory wall thickness, and inlet CO content on temperature and composition profile and heat loss through the wall are studied and discussed in detail.

The following conclusions are derived from the scale-up study:

- The oxygen injection can be further reduced from the calculated excess oxygen; however, this optimization should be considered only when the emission regulations are met.
- Low CO conversion is predicated for lower oxygen injection due to a lower oxygen availability and mixing and also higher local temperature which is detrimental to CO combustion. A minor increase in wall heat loss was predicted for lower oxygen injection.
- Reducing reflux chamber wall thickness leads to a substantial increase in heat loss through the wall which can affect heat recovery performance of design of heat exchanger integrated in the process. However, the wall thickness has a minor effect on CO–H_2–carbon combustion.
- Inlet flue gas CO content has the most considerable effect on flow behavior and reflux chamber performance. Increasing CO content can drastically change the flow temperature, wall temperature, composition profile, and heat loss through the wall since CO is a fuel and the main heat-generating source. Higher inlet CO content will also increase CO emission from reflux chamber.
- The proposed geometry is capable of combusting all unwanted species in a short length of the reflux chamber for all investigated variation of parameters.

ACKNOWLEDGMENTS

This study is part of the Reclamet Project (Nr 17209). The authors would like to thank EIT RawMaterials for funding the project. The authors would like to thank **Sripriya Rajendran** for providing supportive data to this paper.

CONFLICT OF INTEREST

The authors declare that there is no known conflict of interest associated with this publication.

OPEN ACCESS

This article is licensed under a Creative Commons Attribution 4.0 International License, which permits use, sharing, adaptation, distribution and reproduction in any medium or format, as long as you give appropriate credit to the original author(s) and the source, provide a link to the Creative Commons licence, and indicate if changes were made. The images or other third party material in this article are included in the article's Creative Commons licence, unless indicated otherwise in a credit line to the material. If material is not included in the article's Creative Commons licence and your intended use is not permitted by statutory regulation or exceeds the permitted use, you will need to obtain permission directly from the copyright holder. To view a copy of this licence, visit http://creativecommons.org/licenses/by/4.0/.

ABBREVIATIONS

α	Absorption coefficient
Cp	Specific heat of fluid [J/kg. K]
Cp_{eff}	Effective solid specific heat [J/kg. K]
Cps	Specific heat of solid [J/kg. K]
C	Coefficients are constant
d	Tip thickness [m]
D	Base thickness [m]
d_{eff}	Average wall thickness [m]
E	Total energy [J/kg]
$\vec{F}$	Additional force [N]
$\vec{g}$	Gravitational acceleration [m/s^2]
G	Production term
HF	Heat flux [W/m^2]
I	Spectral radiation intensity
$\overrightarrow{J_j}$	Diffusion flux of species
k_{eff}	Effective conductivity of fluid [W/m. K]
k_{s_x}, k_{s_y}, k_{s_z}	Directional solid thermal conductivity [W/m. K]
k_s	Isentropic solid thermal conductivity [W/m. K]
k	Turbulent kinetic energy [m^2/s^2],
m_p	Particle mass [kg]
$m_p \frac{\vec{u}-\vec{u}_p}{\tau_r}$	Drag force [N]
m	Mass flow rate [kg/s]
m_{anchor}	Anchor mass fraction
$m_{refractory}$	Refractory mass fraction
n	Spectral index of refraction of the medium

p	Pressure [Pa]
Q	Heat generation per unit volume [w/m^3]
$\vec{r}$	Position vector [m]
R_i	Net rate of chemical reaction
$\vec{s}$	Direction vector
S_h	Heat of chemical reaction
S	Source term
T	Temperature [K]
T_h	Hot surface temperature [K]
T_c	Outer surface temperature of cooling pipes [K]
t	Time [s]
$\vec{u}_p$	Fluid phase velocity [m/s]
$\vec{u}_p$	Particle velocity [m/s]
u'	Fluctuating velocity [m/s]
$\overline{u}$	Mean velocity [m/s]
Y	Destruction terms

GREEK LETTERS

σ	Stefan–Boltzmann constant
σ_s	Scattering coefficient
Ω'	Solid angle
Γ	Effective diffusivities *[kg/m-s]*
ε	Dissipation frequency *[1/s]*
μ_t	Turbulent viscosity [m^2/s]
μ	Molecular viscosity [kg/m-s]
ρ	Density of fluid [kg/m^3]
ρ_{eff}	Effective density of solid [kg/m^3]
ρ_s	Density of solid [kg/m^3]
ρ_p	Density of the particle [kg/m^3]
τ_r	Particle relaxation time
σ_k	Turbulent Prandtl number for kinetic energy = 1
σ_ε	Turbulent Prandtl number for energy dissipation = 1.2

REFERENCES

1. A. Egedy, S. Fogarasi, T. Varga, Á. Imre-Lucaci, and T. Chován: *Clean Technol. Environ. Policy*, 2015, vol. 17, pp. 1373–80.
2. IEA, Iron and Steel Technology Roadmap, https://www.iea.org/reports/iron-and-steel-technologyroadmap. Accessed 19 Oct 2021.
3. worldsteel, press release, https://www.worldsteel.org/ media-centre/press-releases/2021/Global-crude-steeloutput-decreases-by-0.9–in-2020.html, (Accessed 19 Oct 2021).
4. climate policy, https://www.worldsteel.org/publications/position-papers/climate-change-policy-paper.html, (Accessed 19 Oct 2021).
5. J. Scully, L.B. Considine, M.T. Smith, E. McAlea, N. Jones, E. O'Connell, E. Madsen, M. Power, P. Mellors, J. Crowley, N. O'Leary, S. Carver, and D. Van Plew: *Biotechnol. Bioeng.*, 2020, vol. 117, pp. 1710–23.
6. V. Cappello, C. Plais, C. Vial, and F. Augier: *Chem. Eng. Sci.*, 2021, vol. 229, p. 116033.
7. J.-M. González-Sáiz, D. Garrido-Vidal, and C. Pizarro: *J. Food Eng.*, 2009, vol. 93, pp. 89–100.
8. J. Morchain, J.-C. Gabelle, and A. Cockx: *AIChE J.*, 2014, vol. 60, pp. 27–40.
9. S. Azuhata, K. Narato, H. Kobayashi, N. Arashi, S. Morita, and T. Masai: *Symposium (International) on Combustion*, 1988, vol. 21, pp. 1199–1206.
10. P. Singh, P. Mahanta, and P. Kalita: *Int. Commun. Heat Mass Transfer*, 2021, vol. 128, p. 105590.
11. Y. Cui, W. Zhong, X. Liu, and J. Xiang: *Powder Technol.*, 2021, vol. 394, pp. 103–19.
12. M. Biglari, H. Liu, A. Elkamel, and A. Lohi: *Energies* , 2016, 9, vol. 9.
13. H. Ali, J. Solsvik, J.L. Wagner, D. Zhang, K. Hellgardt, and C.W. Park: *Biotechnol. Bioeng.*, 2019, vol. 116, pp. 2200–11.
14. L. Böhm, L. Hohl, C. Bliatsiou, and M. Kraume: *Chem. Eng. Technol.*, 2019, vol. 91, pp. 1724–46.
15. E. Gavi, D.L. Marchisio, and A.A. Barresi: *Chem. Eng. Sci.*, 2007, vol. 62, pp. 2228–41.
16. J. Gimbun, C.D. Rielly, and Z.K. Nagy: *Chem. Eng. Res. Des.*, 2009, vol. 87, pp. 437–51.
17. W.C. Wilfong, B.W. Kail, Q. Wang, T. Ji, V.A. Kusuma, P. Shah, N. Fusco, S. Yi, F. Shi, and M.L. Gray: *Powder Technol.*, 2022, vol. 395, pp. 243–54.
18. Y. Liu, V. Raman, R.O. Fox, and A.D. Harvey: *Chem. Eng. Sci.*, 2004, vol. 59, pp. 5167–76.
19. Q. Wang, K. Zhang, S. Brandani, and J. Jiang: *Can. J. Chem. Eng.*, 2009, vol. 87, pp. 204–10.
20. J. Parker, K. LaMarche, W. Chen, K. Williams, H. Stamato, and S. Thibault: *Powder Technol.*, 2013, vol. 235, pp. 115–20.
21. X. Liu, D. Hatziavramidis, H. Arastoopour, and A.S. Myerson: *AIChE J.*, 2006, vol. 52, pp. 3621–25.
22. A. Hosseini, V. Dhiman, K. Meijer, C. Zeilstra, J. Hage, T. Peeters, E. Offerman, and Y. Yang: *Ironmaking & Steelmaking*, DOI:https://doi.org/10.1080/03019233.2022.2062929.
23. A.F.U. Guide: 2013.
24. A. Hosseini, R. Calis, D. van der Plas, P. Put, J. Agema, K. Meijer, J.L.T. Hage, E. Offerman, and Y. Yang: *Metallurgical and Materials Transactions B*.
25. B.C. Pak and Y.I. Cho: *Exp. Heat Transfer*, 1998, vol. 11, pp. 151–70.
26. A. Hosseini, V. Dhiman, K. Meijer, C. Zeilstra, J. Hage, T. Peeters, E. Offerman, and Y. Yang: *Ironmak. Steelmak.* https://doi.org/10.1080/03019233.2022.2060457.
27. W. Wagner and A. Pruß: *J. Phys. Chem. Ref. Data*, 2002, vol. 31, pp. 387–535.
28. M.L. Huber, R.A. Perkins, A. Laesecke, D.G. Friend, J.V. Sengers, M.J. Assael, I.N. Metaxa, E. Vogel, R. Mareš, and K. Miyagawa: *J. Phys. Chem. Ref. Data*, 2009, vol. 38, pp. 101–25.
29. M.L. Huber, R.A. Perkins, D.G. Friend, J.V. Sengers, M.J. Assael, I.N. Metaxa, K. Miyagawa, R. Hellmann, and E. Vogel: *J. Phys. Chem. Ref. Data*, 2012, vol. 41, p. 33102.
30. Thermophysical Properties of Water, https://webbook.nist.gov/cgi/fluid.cgi?ID=C7732185&Action=Page, (accessed 10 November 2021).
31. J. Joliff, Y. Belec, L. and Chailan: *Journal of Surface Engineered Materials and Advanced Technology*, 2011, vol. 1, pp. 1–8.

Publisher's Note Springer Nature remains neutral with regard to jurisdictional claims in published maps and institutional affiliations.